

This is the accepted manuscript made available via CHORUS. The article has been published as:

Two-Plasmon Decay Mitigation in Direct-Drive Inertial-Confinement-Fusion Experiments Using Multilayer Targets

R. K. Follett, J. A. Delettrez, D. H. Edgell, V. N. Goncharov, R. J. Henchen, J. Katz, D. T. Michel, J. F. Myatt, J. Shaw, A. A. Solodov, C. Stoeckl, B. Yaakobi, and D. H. Froula

Phys. Rev. Lett. **116**, 155002 — Published 15 April 2016

DOI: [10.1103/PhysRevLett.116.155002](https://doi.org/10.1103/PhysRevLett.116.155002)

Two-plasmon-decay mitigation in direct-drive inertial-confinement-fusion experiments using mid-z layer targets

R. K. Follett,^{1,*} J. A. Delettrez,¹ D. H. Edgell,¹ V. N. Goncharov,¹
R. J. Henchen,¹ J. Katz,¹ D. T. Michel,¹ J. F. Myatt,¹ J. Shaw,¹
A. A. Solodov,¹ C. Stoeckl,¹ B. Yaakobi,¹ and D. H. Froula¹

¹*Laboratory for Laser Energetics, University of Rochester,
250 East River Road, Rochester New York 14623, USA*

(Dated: March 18, 2016)

Abstract

Multilayer direct-drive inertial-confinement-fusion (ICF) targets are shown to significantly reduce two-plasmon-decay (TPD)-driven hot-electron production while maintaining high hydrodynamic efficiency. Implosion experiments on the OMEGA laser used targets with silicon layered between an inner beryllium and outer silicon-doped plastic ablator. A factor-of-5 reduction in hot-electron generation (>50 keV) was observed in the multilayer targets relative to pure CH targets. Three-dimensional simulations of the TPD-driven hot-electron production using a laser-plasma interaction code (*LPSE*) that includes nonlinear and kinetic effects show good agreement with the measurements. The simulations suggest that the reduction in hot-electron production observed in the multilayer targets is primarily caused by increased electron-ion collisional damping.

PACS numbers: 52.35.Fp, 52.35.Mw, 52.35.Qz, 52.38.Kd, 41.75.Jv

In direct-drive inertial confinement fusion (ICF), a cryogenic capsule of deuterium–tritium fuel is imploded by direct laser illumination of a capsule with a thin outer ablator material [1]. The efficiency of laser energy transfer to kinetic energy of the imploding shell (hydrodynamic efficiency) is dependent on the ablator material [2–4] and on the wavelength and intensity of the drive laser. To achieve thermonuclear ignition, the hydrodynamic efficiency of the implosion must be $\gtrsim 5\%$ for MJ scale laser drivers, and less than $\sim 0.1\%$ of the laser energy can be coupled to the cold DT fuel as preheat [5–7].

Preheat reduces the compressibility of the imploding shell. The primary sources of preheat are laser-driven shocks, radiation, and hot electrons ($\gtrsim 50$ keV). Preheat from shocks is mitigated by driving the capsule with a series of properly timed weak shocks driven by a temporally shaped laser pulse. The ablator material is chosen to balance laser absorption, hydrodynamic efficiency, and radiation preheat. Both the ablation pressure and the mass ablation rate increase with the ratio of the atomic mass to the atomic number (A/Z) [8], while collisional laser absorption and radiation preheat increase with atomic number (Z).

The dominant source of hot electrons [9] in ICF implosions is large-amplitude electron plasma waves (EPWs) driven by the stimulated Raman scattering (SRS) and two-plasmon–decay (TPD) instabilities [5, 6, 10]. A single plane-wave linear-stability analysis gives a threshold for absolute TPD growth of $I\lambda_\mu L_n/82T_e = 1$ (where I is the laser intensity in 10^{14} W/cm², λ_μ is the laser wavelength in microns, L_n is the density scalelength in microns, and T_e is the electron temperature in keV) [11, 12].

Two-plasmon decay and SRS driven hot-electron production were major deterrents to the success of early ICF experiments that used 1- μ m wavelength lasers [13, 14]. The development of frequency conversion enabled the use of 0.351- μ m lasers that reduced the single-beam instabilities to below threshold, but the TPD instability is still predicted to be well above threshold in current direct-drive ICF designs because of the ability of multiple coherent overlapping laser beams ($I \sim 10^{15}$ W/cm²) to couple to common EPWs [15–17]. In typical direct-drive ICF experiments, $\sim 1\%$ of the incident laser energy is coupled into hot electrons [18]. These levels of hot-electron production are likely to lead to untenable preheat for successful ICF ignition using conventional CH capsules.

To limit the growth of these instabilities and mitigate hot-electron production, adding multiple material layers in the target has been proposed [19]. Figure 1(a) shows an ignition-scalable target designed to mitigate TPD while minimizing radiation preheat and taking

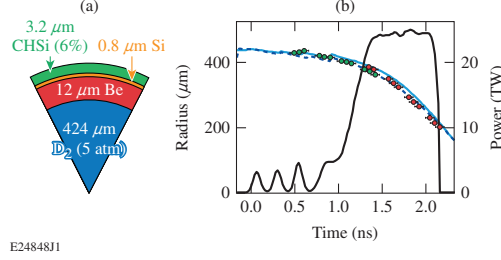


FIG. 1: (a) Cross section of multilayer target. (b) Measured implosion trajectories from two separate x-ray framing cameras (red and green circles) with *LILAC*-simulated trajectories for the multilayer target (solid line) and CH target with the drive-beam intensity increased by 20% (dashed line). The pulse shape is shown in black.

advantage of the high hydrodynamic efficiency of beryllium. The silicon layer increases the coronal plasma temperature, decreases the density scalelength, and increases the electron-ion collisional damping [$\nu_{ei} \propto \langle Z^2 \rangle / (\langle Z \rangle T^{3/2})$] relative to CH at the times when the TPD growth rates are largest [20].

This Letter presents the first observations of hot-electron mitigation and an increased hydrodynamic efficiency in direct-drive implosions using mid-z layer targets. A factor-of-5 reduction in hot-electron generation (>50 keV) was observed in multilayer targets relative to pure CH targets. Temporally and spatially resolved ultraviolet Thomson-scattering measurements of ion-acoustic and electron plasma waves show increased electron temperatures in the coronal plasma for the multilayer target compared with CH targets. Three-dimensional laser-plasma interaction simulations of the hot-electron production are in good agreement with the temporally resolved hot-electron measurements, including the significant reduction of hot-electron production observed in the multilayer targets. The simulations show that in addition to the reduced gain (smaller IL_n/T_e), the observed reduction in hot electrons results from increased electron-ion collision frequencies and reduced Landau damping of ion-acoustic waves.

The experiments were conducted on the OMEGA Laser Facility [21] and used 60 laser beams ($\lambda_{3\omega} = 351$ nm) focused onto 860- μm -diam spherical targets to produce peak overlapped intensities of $\sim 10^{15}$ W/cm² in a 2.4-ns shaped pulse with three 100-ps picket pulses [Fig. 1(b)]. Distributed phase plates [22] were used on each beam to define the 790- μm full-width-at-half-maximum (FWHM) flat-top laser spots at best focus of the $f/6.7$ lenses. Three different types of mass-equivalent spherical shell targets filled with 5 atm of D_2 gas were used. The shell thicknesses were 27 μm for the CH, 14 μm for the Be, and 12 μm (Be),

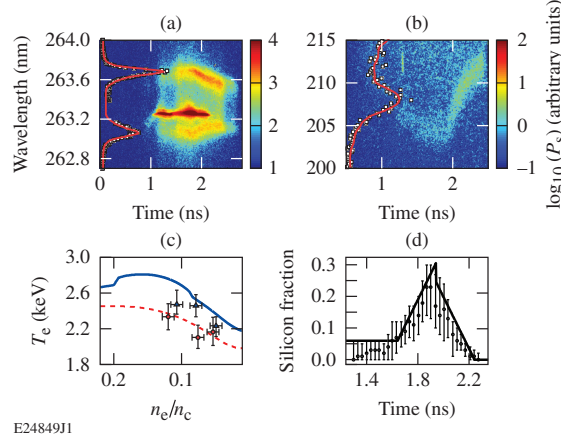


FIG. 2: Thomson-scattering spectra from (a) IAWs and (b) EPWs in a multilayer target implosion taken $200\ \mu\text{m}$ from the initial target surface with fits (lines) to spectral lineouts (squares) overlaid. The bright feature at around $263.2\ \text{nm}$ between the two ion-acoustic peaks corresponds to probe-beam light either refracted or specularly reflected in the Thomson-scattering diagnostic and was not included in the fits. (c) Simulated (curves) and measured (markers) electron temperatures as a function of density (at $1.9\ \text{ns}$) for the CH (red) and multilayer (blue) targets. (d) Atomic fraction of silicon present in the Thomson-scattering volume inferred from the measurements (circles) and assuming a mass-conserving triangle function (solid curve). The error bars correspond to a 20% increase in χ^2 .

$0.8\ \mu\text{m}$ (Si), $3.5\ \mu\text{m}$ (CH doped with 6% Si) for the multilayer targets [Fig. 1(a)].

Figure 1(b) shows the measured and simulated implosion trajectory for the multilayer target [8]. To show the increased hydrodynamic efficiency of the multilayer targets, the multilayer implosion trajectory is compared to the simulated trajectory of a CH target with the incident laser energy increased by 20% to match the multilayer trajectory. Although the laser absorption is slightly higher in the multilayer targets, the primary source of the increased hydrodynamic efficiency in the multilayer targets relative to the CH targets is the increased ablation pressure in the beryllium. This is apparent from the fact that the beryllium targets had similar implosion trajectories to the multilayer targets despite having the lowest laser absorption. The implosions were simulated using the 1-D radiation-hydrodynamics code *LILAC* [23] with cross-beam energy transfer (CBET) [24] and nonlocal thermal-transport models [25]. The implosion trajectories were measured using self-emission shadowgraphy [26].

For the highest intensity shots, the neutron yields in the multilayer ($5.33 \pm 0.04 \times 10^{10}$) and beryllium ($5.69 \pm 0.05 \times 10^{10}$) targets were nearly a factor-of-2 higher than in CH targets ($2.89 \pm 0.04 \times 10^{10}$). This shows that the multilayer target imploded as efficiently as the

beryllium target and suggests that the multilayer ablator did not significantly reduce the hydrodynamic stability of the implosion. The observed increase in neutron yield in the beryllium and multilayer targets relative to CH targets was predicted to result primarily from their increased hydrodynamic efficiency. The similarity in neutron yield between the beryllium and multilayer targets suggests that TPD preheat did not significantly degrade these implosions.

Ultraviolet Thomson scattering was used to measure the coronal plasma conditions. The Thomson-scattering diagnostic consisted of a $\lambda_{4\omega} = 263.25\text{-nm}$ $f/6.7$ probe beam with a best-focus diameter of $\sim 70\mu\text{m}$ [27]. The Thomson-scattered light was collected by a reflective $f/10$ collection system coupled to two spectrometer/streak cameras, used to simultaneously observe the EPW and ion-acoustic wave (IAW) scattering features [28]. Scattered light was collected from an $\sim 50 \times 50 \times 70\text{-}\mu\text{m}^3$ volume located 200 to 400 μm from the initial target surface. The angle between the collection optic and probe beam was 120° . To avoid the possibility of probe light being refracted directly into the collection optic, the Thomson-scattering diagnostic was configured to probe wave vectors perpendicular to the target normal.

Figure 2 shows simultaneous measurements of IAW and EPW Thomson-scattering spectra. The plasma conditions in the Thomson-scattering volume were inferred using chi-squared fits to the kinetic multispecies dynamic structure factor assuming Maxwellian ion and electron velocity distributions [29]. The densities and temperatures were inferred independently from fits to the EPW and IAW spectra, respectively. The Thomson-scattering volume and probed wave vector were calculated using 3-D ray tracing [30] of the simulated plasma profiles, and the calculated spatial and temporal (from the $\sim 70\text{-ps}$ instrument response and 50-ps lineout averaging) gradients were included in the fits [31].

Figure 2(c) shows simulated and measured electron temperatures as a function of density for the multilayer and CH targets. The Thomson-scattering measurements are in good agreement with the simulations and show the increased electron temperature in the coronal plasma of the multilayer target. The bump in electron temperature in the multilayer plasma corresponds to the Si layer propagating outward through the corona.

Figure 2(d) shows the inferred silicon fraction as a function of time, which rises roughly linearly with time and persists for $\sim 0.6\text{ ns}$. To model the silicon fraction, it was assumed the layer of pure silicon diffused symmetrically into the CH and beryllium layers. The solid line

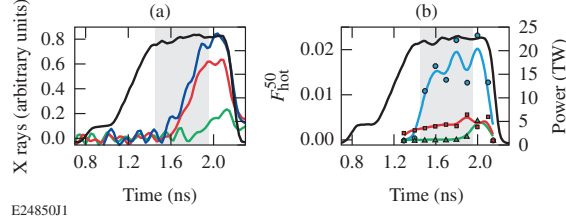


FIG. 3: (a) Measured hard x-ray power above ~ 50 keV for CH (blue line), Be (red line), and multilayer (green line) targets. (b) *LPSE*-simulated fractions of laser energy converted into >50 keV electrons for CH (blue circles), Be (red squares), and multilayer (green triangles) targets. The lines represent the *LPSE* simulated points convolved with the 100-ps instrument response. The gray region shows the range of times that silicon is present at $n_c/4$. The pulse shape is shown in black.

in Fig. 2(d) is the expected (mass-conserving) silicon fraction assuming a triangle function with a full width of 0.6 ns. The center of the silicon distribution was placed at the time where the silicon was calculated by the hydrodynamic simulations to pass through the scattering volume. It was necessary to assume some hydrogen mix throughout the duration of the probe to reproduce the width of the observed spectral peaks. This approximation was justified on the basis of the large hydrogen mean-free-path ($\lambda_{ii} \equiv v_{ti}/\nu_{ii} \approx 5 \mu\text{m}$ at near-quarter-critical densities, which is $\sim 100\times$ the mean-free-path of silicon). Other possible sources of mix are the Rayleigh-Taylor instability at the initially unstable Be/Si interface and the large gradient in electron density created when ionizing the CH/Si and Be/Si interfaces.

The hot-electron generation was inferred by measuring hard x-rays [32]. The absolute hard x-ray spectrum generated by bremsstrahlung emission from hot electrons was measured using a nine-channel time-integrated, image-plate-based hard-x-ray detector (HXIP) [33]. The time-resolved hard x-rays above ~ 50 keV were measured using a scintillator-based hard x-ray detector (HXRD) [34].

Figure 3(a) shows a significant reduction in the hard x-rays generated by hot electrons in the multilayer targets compared with the CH or Be targets. In the CH and beryllium targets, the onset of hot-electron production is at ~ 1.6 ns, while in the multilayer targets the onset is delayed to ~ 1.9 ns. This corresponds with the time that the silicon has passed through the quarter-critical density surface [Fig. 2(d)], suggesting that the silicon effectively mitigates TPD.

Figure 3(b) shows the calculated hot-electron (>50 keV) production as a function of time from TPD simulations of the three different targets. The calculated relative hot-electron

production between the three targets confirms the TPD-mitigating properties of the silicon layer. Consistent with the measurements, the majority of the hot-electron production in the multilayer targets occurs after the silicon has passed through the quarter critical region. Because the TPD simulation results shown in Fig. 3(b) assumed steady-state coronal plasma conditions, the earlier onset of hot-electron production in the simulations relative to the experiments could result from the rapidly changing hydrodynamic conditions following the rise of the main laser pulse.

The TPD-driven hot-electron production was simulated using a 3-D nonlinear plasma fluid code (*LPSE* [35]) that is coupled to a particle solver that self-consistently evolves the electron velocity distribution in the calculated electrostatic fields. This modified electron velocity distribution is used to calculate the hot-electron fraction and Landau damping of EPWs. *LPSE* solves the extended Zakharov equations of TPD [36, 37] for the low-frequency IAWs and high-frequency (enveloped) EPWs. The extended Zakharov equations include terms for the linear coupling between the drive beams and electrostatic perturbations (TPD, ponderomotive force) and nonlinear terms for the coupling between EPWs and IAWs (Langmuir decay, profile steepening, turbulence) [20]. *LPSE* has realistic Landau damping and Braginskii [38] electron-ion collisional damping. Landau damping of IAWs was calculated from the kinetic electron (χ_e) and ion (χ_i) susceptibilities assuming a Maxwellian unperturbed velocity distribution ($\omega_i = \text{Im}[\epsilon/(\partial\epsilon/\partial\omega)]$, where $\epsilon = 1 + \chi_e + \chi_i$) [39]. The simulation box was $\sim 70 \times 13 \times 13 \mu\text{m}^3$ on a uniform $1024 \times 256 \times 256$ Cartesian grid. The *LPSE* simulations were run until a statistical steady state was achieved (~ 40 ps).

Figure 4 shows the hot-electron fractions (>50 keV) inferred from the HXIP diagnostic at three different drive beam intensities. In all cases, the multilayer targets generated less hot electrons. For the shots with laser intensities $\sim 10^{15}$ W/cm², the multilayer target had 5.4 (3.1) \times less hot-electron production than the CH (Be) target. The *LPSE* simulated hot-electron fractions were multiplied by a factor of 3 to show the qualitative agreement between the simulated and measured hot-electron production for the three target types. Figure 4 shows that *LPSE* predicts the multilayer target to be close to threshold at the lowest intensity, while the beryllium and CH targets are not. The large discrepancy in hot-electron fraction between *LPSE* and experiment for the multilayer target at the lowest intensity is because, while both are close to the instability threshold, the experiment is higher above it than predicted. By comparison with the existing data base (e.g., Ref. [40]), a reduction in

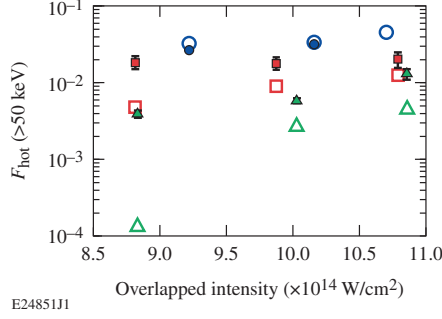


FIG. 4: The measured (solid markers) and simulated (open markers) fraction of incident laser energy converted into hot electrons (>50 keV) for CH (circles), beryllium (squares), and multilayer (triangles) targets as a function of drive beam intensity. The simulated hot-electron fractions have been multiplied by a factor of 3 to show the relative agreement with the measurements. The error bars correspond to statistical error (the absolute error is a factor of ~ 2 , primarily a result of image plate calibration and calculating the hot-electron to x-ray conversion).

the experimental intensity by $<30\%$ would be required for agreement. The LPSE simulations do reproduce the relative ordering of hot-electron production in the different targets. These results are far from trivial—the instability results from the cooperative action of multiple smoothed beams in inhomogeneous plasma and the hot-electron production mechanisms are highly nonlinear. Knowledge of the interaction conditions contains uncertainties that could account for 30% offsets in threshold.

The addition of the silicon layer in the multilayer target mitigates TPD through all of the linear mechanisms discussed in the introduction (decreased IL_n/T_e and increased electron-ion collisional damping) and through nonlinear mechanisms governed by the Landau damping of IAWs (decreased $\nu_i^{\text{LD}} \propto T_i/ZT_e$). Reducing the Landau damping of IAWs increases the transfer of energy from TPD-driven EPWs to IAWs via the Langmuir decay instability, which limits the amplitude of the EPWs and consequently inhibits hot-electron generation.

To compare the relative importance of the various TPD suppression mechanisms, the Landau damping of IAWs, electron-ion collisional damping, and the hydrodynamic conditions in the CH simulations were systematically modified to match the multilayer simulations (at 1.7 ns). The largest reduction in hot-electron production was observed when varying the electron-ion collision frequency (factor-of-70 reduction). The second-largest change occurred when varying the hydrodynamic conditions (factor-of-10 reduction). The Landau damping of IAWs had the weakest effect (factor-of-4 reduction).

The primary source of TPD mitigation in the beryllium simulations is the reduced ion Landau damping relative to CH. The density scalelength was longer and the electron temperature slightly lower in the beryllium targets relative to the CH targets, which means that the TPD gains predicted by linear theory are higher in the beryllium than in the CH. Beryllium also has less electron-ion collisional damping than CH because of its lower $Z_{\text{eff}} \equiv \langle Z^2 \rangle / \langle Z \rangle$. The only parameter that is beneficial to the beryllium targets in terms of TPD mitigation is low ion Landau damping, which was almost an order of magnitude lower than in the CH. Increasing the ion Landau damping in the beryllium *LPSE* simulation to match the CH simulation resulted in a factor-of-3 increase in hot-electron production.

In summary, multilayer targets were shown to significantly reduce hot-electron production while maintaining high hydrodynamic efficiency. Measurements of TPD driven hot-electron divergence [41] suggest that the observed factor-of-5 reduction in hot-electron production reduced the preheat in these experiments from $\sim 0.6\%$ in CH to $\sim 0.12\%$ in the multilayer target. The good agreement between the *LPSE* simulated and measured hot-electron production suggests that *LPSE* calculations accurately reproduce the physics of TPD growth and saturation. The ability to simulate the relative impact of various TPD saturation mechanisms allows for further improvement of hot-electron mitigation strategies in ICF implosions. These results suggest that a multilayer direct-drive-ignition target could be used to mitigate TPD by (1) using an inner Be layer to increase the hydrodynamic efficiency, allowing the quarter-critical intensity to be reduced by $\sim 20\%$ while maintaining the implosion velocity and (2) using a silicon layer near the quarter-critical surface to increase the electron temperature, reduce the density scalelength, increase electron-ion collisional damping, and reduce the threshold for Langmuir decay of TPD-driven EPWs.

This material is based upon work supported by the Department of Energy National Nuclear Security Administration under Award Number DE-NA0001944, the University of Rochester, and the New York State Energy Research and Development Authority. The support of DOE does not constitute an endorsement by the DOE of the views expressed in this article.

* Electronic address: rfollett@lle.rochester.edu

[1] S. Atzeni and J. Meyer-ter Vehn, *The Physics of Inertial Fusion: Beam Plasma Interaction*,

- Hydrodynamics, Hot Dense Matter*, International Series of Monographs on Physics (Clarendon Press, Oxford, 2004).
- [2] W. M. Manheimer, D. G. Colombant, and J. H. Gardner, *Phys. Fluids* **25**, 1644 (1982).
 - [3] P. Mora, *Phys. Fluids* **25**, 1051 (1982).
 - [4] C. E. Max, C. F. McKee, and W. C. Mead, *Phys. Fluids* **23**, 1620 (1980).
 - [5] V. A. Smalyuk, D. Shvarts, R. Betti, J. A. Delettrez, D. H. Edgell, V. Y. Glebov, V. N. Goncharov, R. L. McCrory, D. D. Meyerhofer, P. B. Radha, et al., *Phys. Rev. Lett.* **100**, 185005 (2008).
 - [6] B. Yaakobi, C. Stoeckl, W. Seka, J. A. Delettrez, T. C. Sangster, and D. D. Meyerhofer, *Phys. Plasmas* **12**, 062703 (2005).
 - [7] R. L. McCrory, D. D. Meyerhofer, R. Betti, R. S. Craxton, J. A. Delettrez, D. H. Edgell, V. Y. Glebov, V. N. Goncharov, D. R. Harding, D. W. Jacobs-Perkins, et al., *Phys. Plasmas* **15**, 055503 (2008).
 - [8] D. T. Michel, V. N. Goncharov, I. V. Igumenshchev, R. Epstein, and D. H. Froula, *Phys. Rev. Lett.* **111**, 245005 (2013).
 - [9] N. A. Ebrahim, H. A. Baldis, C. Joshi, and R. Benesch, *Phys. Rev. Lett.* **45**, 1179 (1980).
 - [10] W. L. Kruer, *The Physics of Laser Plasma Interactions* (Addison-Wesley, Redwood City, CA, 1988).
 - [11] A. Simon, R. W. Short, E. A. Williams, and T. Dewandre, *Phys. Fluids* **26**, 3107 (1983).
 - [12] M. N. Rosenbluth, *Phys. Rev. Lett.* **29**, 565 (1972).
 - [13] R. S. Craxton, K. S. Anderson, T. R. Boehly, V. N. Goncharov, D. R. Harding, J. P. Knauer, R. L. McCrory, P. W. McKenty, D. D. Meyerhofer, J. F. Myatt, et al., *Phys. Plasmas* **22** (2015).
 - [14] J. D. Lindl, P. Amendt, R. L. Berger, S. G. Glendinning, S. H. Glenzer, S. W. Haan, R. L. Kauffman, O. L. Landen, and L. J. Suter, *Phys. Plasmas* **11**, 339 (2004).
 - [15] C. Stoeckl, R. E. Bahr, B. Yaakobi, W. Seka, S. P. Regan, R. S. Craxton, J. A. Delettrez, R. W. Short, J. Myatt, A. V. Maximov, et al., *Phys. Rev. Lett.* **90**, 235002 (2003).
 - [16] D. T. Michel, A. V. Maximov, R. W. Short, S. X. Hu, J. F. Myatt, W. Seka, A. A. Solodov, B. Yaakobi, and D. H. Froula, *Phys. Rev. Lett.* **109**, 155007 (2012).
 - [17] R. K. Follett, D. H. Edgell, R. J. Henchen, S. X. Hu, J. Katz, D. T. Michel, J. F. Myatt, J. Shaw, and D. H. Froula, *Phys. Rev. E* **91**, 031104 (2015).

- [18] D. H. Froula, I. V. Igumenshchev, D. T. Michel, D. H. Edgell, R. Follett, V. Y. Glebov, V. N. Goncharov, J. Kwiatkowski, F. J. Marshall, P. B. Radha, et al., Phys. Rev. Lett. **108**, 125003 (2012).
- [19] V. N. Goncharov, T. C. Sangster, R. Betti, T. R. Boehly, M. J. Bonino, T. J. B. Collins, R. S. Craxton, J. A. Delettrez, D. H. Edgell, R. Epstein, et al., Phys. Plasmas **21**, 056315 (2014).
- [20] J. F. Myatt, H. X. Vu, D. F. DuBois, D. A. Russell, J. Zhang, R. W. Short, and A. V. Maximov, Phys. Plasmas **20**, 052705 (2013).
- [21] T. R. Boehly, R. S. Craxton, T. H. Hinterman, J. H. Kelly, T. J. Kessler, S. A. Kumpan, S. A. Letzring, R. L. Mccrory, S. F. B. Morse, W. Seka, et al., Rev. Sci. Instrum. **66**, 508 (1995).
- [22] T. J. Kessler, Y. Lin, J. Armstrong, and B. Velazquez, *Phase Conversion of Lasers with Low-Loss Distributed Phase Plates*, vol. 1870 of *Laser Coherence and Control: Technology and Applications* (SPIE, Bellingham, WA, 1993).
- [23] J. Delettrez, R. Epstein, M. C. Richardson, P. A. Jaanimagi, and B. L. Henke, Phys. Rev. A **36**, 3926 (1987).
- [24] I. V. Igumenshchev, D. H. Edgell, V. N. Goncharov, J. A. Delettrez, A. V. Maximov, J. F. Myatt, W. Seka, A. Shvydky, S. Skupsky, and C. Stoeckl, Phys. Plasmas **17**, 122708 (2010).
- [25] V. N. Goncharov, T. C. Sangster, T. R. Boehly, S. X. Hu, I. V. Igumenshchev, F. J. Marshall, R. L. McCrory, D. D. Meyerhofer, P. B. Radha, W. Seka, et al., Phys. Rev. Lett. **104**, 165001 (2010).
- [26] D. T. Michel, C. Sorce, R. Epstein, N. Whiting, I. V. Igumenshchev, R. Jungquist, and D. H. Froula, Rev. Sci. Instrum. **83**, 10E530 (2012).
- [27] A. J. Mackinnon, S. Shiromizu, G. Antonini, J. Auerbach, K. Haney, D. H. Froula, J. Moody, G. Gregori, C. Constantin, C. Sorce, et al., Rev. Sci. Instrum. **75**, 3906 (2004).
- [28] J. Katz, R. Boni, C. Sorce, R. Follett, M. J. Shoup III, and D. H. Froula, Rev. Sci. Instrum. **83**, 10E349 (2012).
- [29] D. H. Froula, S. H. Glenzer, N. C. Luhmann, and J. Sheffield, *Plasma Scattering of Electromagnetic Radiation: Theory and Measurement Techniques* (Academic Press, Burlington, MA, 2011), 2nd ed.
- [30] R. S. Craxton and R. L. McCrory, J. Appl. Phys. **56**, 108 (1984).
- [31] T. E. Tierney IV, D. S. Montgomery, J. F. Benage, Jr., F. J. Wysocki, and M. S. Murillo, J. Phys. A **36**, 5981 (2003).

- [32] B. Yaakobi, P. Y. Chang, A. Solodov, C. Stoeckl, D. H. Edgell, R. S. Craxton, S. X. Hu, J. F. Myatt, F. J. Marshall, W. Seka, et al., *Phys. Plasmas* **19**, 012704 (2012).
- [33] A. A. Solodov, B. Yaakobi, D. H. Edgell, R. K. Follett, C. Sorce, and D. H. Froula, “Measurements of Fast-Electron Temperature in Laser-Irradiated Plasmas,” submitted to *Physics of Plasmas* (2016).
- [34] C. Stoeckl, V. Y. Glebov, D. D. Meyerhofer, W. Seka, B. Yaakobi, R. P. J. Town, and J. D. Zuegel, *Rev. Sci. Instrum.* **72**, 1197 (2001).
- [35] J. F. Myatt, J. G. Shaw, V. N. Goncharov, J. Zhang, A. V. Maximov, R. W. Short, R. K. Follett, W. Seka, D. H. Edgell, and D. H. Froula, “Laser–Plasma Interaction in Direct-Drive Inertial Confinement Fusion,” submitted to *Journal of Physics: Conference Series*. (2015).
- [36] D. F. DuBois, D. A. Russell, and H. A. Rose, *Phys. Rev. Lett.* **74**, 3983 (1995).
- [37] D. A. Russell and D. F. DuBois, *Phys. Rev. Lett.* **86**, 428 (2001).
- [38] S. I. Braginskii, in *Reviews of Plasma Physics*, edited by A. M. A. Leontovich (Consultants Bureau, New York, 1965), vol. 1, p. 205.
- [39] D. A. Gurnett and A. Bhattacharjee, *Introduction to Plasma Physics: With Space and Laboratory Applications* (Cambridge University Press, 2005).
- [40] D. T. Michel, A. V. Maximov, R. W. Short, J. A. Delettrez, D. Edgell, S. X. Hu, I. V. Igumenshchev, J. F. Myatt, A. A. Solodov, C. Stoeckl, et al., *Phys. Plasmas* **20**, 055703 (2013).
- [41] B. Yaakobi, A. A. Solodov, J. F. Myatt, J. A. Delettrez, C. Stoeckl, and D. H. Froula, *Phys. Plasmas* **20** (2013).